

Clock spectroscopy of interacting bosons in deep optical lattices

R. Bouganne,^{1,*} M. Bosch Aguilera,^{1,*} A. Dareau,^{1,†} E. Soave,^{1,‡} J. Beugnon,¹ and F. Gerbier^{1,§}

¹*Laboratoire Kastler Brossel, Collège de France, CNRS, ENS-PSL Research University, UPMC-Sorbonne Universités, 11 place Marcelin Berthelot, 75005 Paris, France*

(Dated: July 21, 2022)

We report on high-resolution optical spectroscopy of interacting bosonic ^{174}Yb atoms in deep optical lattices with negligible tunneling. We prepare Mott insulator phases with singly- and doubly-occupied isolated sites and probe the atoms using an ultra-narrow “clock” transition. Atoms in singly-occupied sites undergo long-lived Rabi oscillations. Atoms in doubly-occupied sites are strongly affected by interatomic interactions, and we measure their inelastic decay rates and energy shifts. We deduce from these measurements all relevant collisional parameters involving both clock states, in particular the intra- and inter-state scattering lengths.

I. INTRODUCTION

In the last decade, progress in laser frequency stabilization and frequency comparison has led to a new generation of atomic clocks with unprecedented performances [1]. These clocks use ultra-narrow optical transitions (hereafter “clock” transitions), interrogated with ultra-stable lasers locked to high-finesse Fabry-Perot cavities. Because such optical transitions are essentially free of spontaneous emission, they provide new opportunities not only for frequency metrology, but also for quantum information processing [2, 3], many-body physics and quantum simulation [4–6]. For instance, spin-orbit coupling has been demonstrated in ^{87}Sr [7] and ^{173}Yb atoms [8]. While atomic interactions are usually detrimental in frequency metrology [1], they play an important part in the study of quantum gases or the generation of entanglement. Interactions can be precisely characterized using clock transitions. Recently, large spin exchange interactions have been measured with fermionic ^{173}Yb [9, 10], which is promising for the simulation of quantum impurity models. In return, degenerate quantum gases may help to improve the accuracy of optical clocks by offering a better control over interaction effects [1], as suggested by a recent demonstration with a degenerate Fermi gas of ^{87}Sr [11]. Most optical clocks currently operate with fermionic atoms, which reduces but does not eliminate the problem of interactions at low temperatures [12]. However, bosonic atoms could provide advantages due to their reduced sensitivity to external fields and simpler level structure, or for comparing clocks based on different isotopes [1]. Interaction effects could be essentially eliminated using many-body correlated states, *e.g.* a Mott insulator with one atom per lattice site.

In this work, we report on a spectroscopic study of such a bosonic Mott insulator of ^{174}Yb using an ultra-narrow clock transition. A typical experimental result is shown in Fig. 1b. Starting from a sample in the ground state $g \equiv ^1S_0$, we switch on at time $t = 0$ a coupling laser resonant on the clock transition. This triggers coherent oscillations between g and the metastable excited state $e \equiv ^3P_0$. After a fast initial decay of the total atom number, the contrast of the oscillations approaches unity and eventually decreases for $t \gtrsim 5$ ms. This behavior can be understood by considering the initial distribution of atoms in a trapped Mott insulator, made of extended regions of uniform integer filling with 1 or 2 atoms per site (the so-called “Mott plateaus” [13]). While singly-occupied sites undergo coherent Rabi oscillations, doubly-occupied sites are strongly affected by inelastic and elastic interactions, the former explaining the initial decay. In this article, we analyze in detail these features, and show that they can be used for the precise measurement of previously unknown collisional properties of ^{174}Yb .

The paper is organized as follows. We describe the experimental setup in II, including the sequence used to prepare an ultracold bosonic gas in an optical lattice in Section II A, and the optical setup for the clock laser and detection scheme in II B. We present a measurement of the on-site occupation numbers in the Mott insulator phase in Section II C. In III, we analyze the dynamics of doubly-occupied sites. Using the model presented in III A, we extract inelastic (III B) and elastic (III C) interaction parameters from spectroscopic data. We conclude in IV.

II. EXPERIMENTAL SETUP AND METHODS

A. A Mott insulator of bosonic ytterbium atoms

1. Optical lattice setup

Our experiment starts with a nearly pure Bose-Einstein condensate (BEC) of about 10^5 ^{174}Yb atoms in a crossed optical dipole trap (CDT) with initial trap

* RB and MBA contributed equally to this work.

† Present address: Vienna Center for Quantum Science and Technology, TU Wien Atominstitut, Stadionallee 2, 1020 Vienna, Austria

‡ Present address: Institut für Experimentalphysik, Universität Innsbruck, 6020 Innsbruck, Austria

§ fabrice.gerbier@lkb.ens.fr

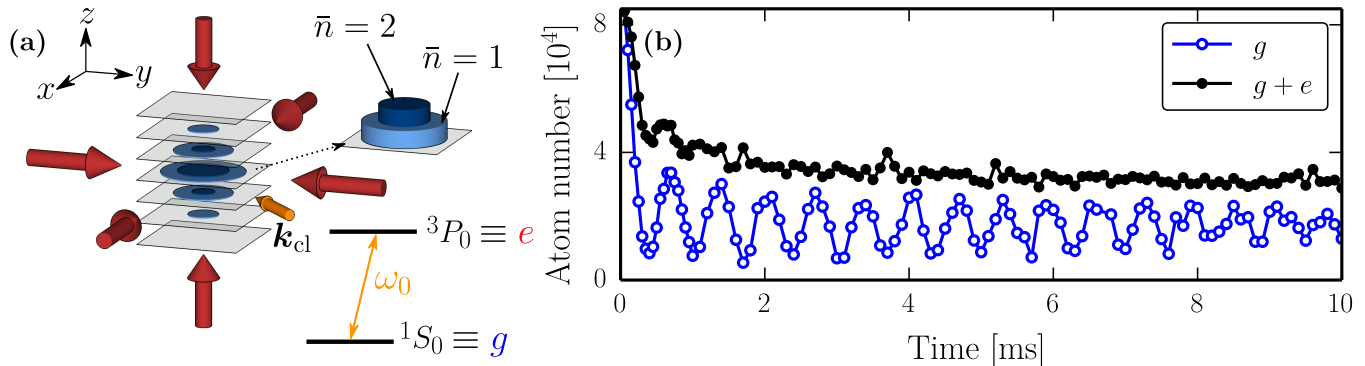


FIG. 1. (a) Sketch of the three-dimensional lattice geometry. The drawing also illustrates the density profile of the Mott insulator and the level scheme of the ultra-narrow clock transition connecting the ground state g and the metastable excited state e . (b) Coherent oscillations on the clock transition in the deep Mott insulator regime. A coupling laser resonant on the clock transition is switched on at time $t = 0$. Closed (respectively open) symbols represent the remaining total atom number (resp. the population in the ground state g).

frequencies $\{\omega_x, \omega_y, \omega_z\} = 2\pi \times \{60 \text{ Hz}, 230 \text{ Hz}, 260 \text{ Hz}\}$ (see [14, 15] for more details). The BEC is transferred into a three-dimensional cubic optical lattice depicted in Fig. 1a. This lattice results from the incoherent superposition of three orthogonal standing waves with orthogonal polarizations [13]. All lattice light beams derive from the same laser operating at the magic wavelength $\lambda_m \approx 759.4 \text{ nm}$ [1, 16], for which the polarizabilities of g and e are equal [17]. The periodic optical lattice potential experienced by the atoms irrespective of their internal state is then

$$V_{\text{OL}} = \sum_{\alpha=x,y,z} V_{0,\alpha} \sin^2(k_m \alpha), \quad (1)$$

where $V_{0,\alpha}$ are the lattice depths and where $k_m = 2\pi/\lambda_m$ is the lattice wavenumber. We calibrate the lattice depths $V_{0,\alpha}$ for given laser powers by Kapitza-Dirac diffraction. The vertical lattice (VL) depth $V_{0,z} \approx 27 E_R$ is essentially fixed (see Section II A 2), while the horizontal lattice (HL) depths can be varied from zero to $\{V_{0,x}, V_{0,y}\} \approx \{24, 25.4\} E_R$. Here $E_R = \hbar^2 k_m^2 / 2M$ is the recoil energy, with M the atomic mass. In this work, unless stated explicitly, we use the largest available lattice depths. The Gaussian envelope of the lattice lasers also entails an additional, slowly varying harmonic potential

$$V_T = \sum_{\alpha=x,y,z} \frac{1}{2} M \Omega_\alpha^2 \alpha^2. \quad (2)$$

By recording collective mode frequencies of a BEC, we infer the Gaussian beam waists for each standing wave, $\{w_x, w_y, w_z\} \approx \{115 \mu\text{m}, 125 \mu\text{m}, 150 \mu\text{m}\}$. The corresponding trap frequencies are $\{\Omega_x, \Omega_y, \Omega_z\} = 2\pi \times \{42 \text{ Hz}, 38 \text{ Hz}, 33 \text{ Hz}\}$ for lattice depths $\{V_{0,x}, V_{0,y}, V_{0,z}\} = \{24, 25.4, 27\} E_R$.

2. Adiabatic preparation of a Mott insulator

The BEC is transferred into the optical lattice in three consecutive steps, aiming at preparing a stack of independent 2D Bose gases in the lowest Bloch band of the HL: (i) a fast ramp up of the VL, (ii) a slow extinction of the CDT and (iii) an adiabatic increase of the HL.

In more detail, we first ramp up in 20 ms a single standing wave propagating vertically (VL), superimposed on the CDT. This fast increase is used to freeze the vertical motion in the combined potential formed by the optical lattice and gravity. The potential V_T alone barely traps the atoms along gravity with a sag of the cloud much larger than in the CDT ($\Delta z_T = g_0/\Omega_z^2 \approx 230 \mu\text{m}$ compared to $\Delta z_{\text{CDT}} = g_0/\omega_z^2 \approx 4 \mu\text{m}$, respectively, with g_0 the acceleration of gravity). The fast ramp up of the VL (as opposed to a slow, quasi-adiabatic transfer) prevents from inducing any motion along z , potentially leading to heating of the cloud [18]. Note, however, that the duration of this first step is still long enough to avoid inter-band transitions. In a second step, the CDT is smoothly extinguished in 200 ms to create a stack of independent two-dimensional condensates in the VL potential alone. This step reduces the atomic density and hence mitigates the rate of three-body losses. It also avoids differential light shifts between the clock states created by the CDT lasers. In a final step, the two arms of the HL are increased to their desired values in 100 ms, which roughly fulfills the criterion of [19] for adiabatic loading of the lowest Bloch band.

Each planar gas can be described by a 2D Bose-Hubbard Hamiltonian [13]

$$\hat{H} = - \sum_{\langle i,j \rangle_\perp} J_\perp \hat{a}_{g,j}^\dagger \hat{a}_{g,i} + \sum_{i_\perp} \frac{U_{gg}}{2} \hat{n}_i (\hat{n}_i - 1) + \sum_{i_\perp} \frac{M}{2} (\Omega_x^2 x_i^2 + \Omega_y^2 y_i^2) \hat{n}_i. \quad (3)$$

Here the notation i_{\perp} indicates summation over all lattice sites at positions $\boldsymbol{\rho}_i = (x_i, y_i)$ in the $x - y$ plane, and $\langle i, j \rangle_{\perp}$ in-plane tunneling to nearest-neighbors with matrix element J_{\perp} . Tunneling along the gravity direction has been neglected. The on-site energy U_{gg} is given by

$$U_{gg} = \frac{4\pi\hbar^2 a_{gg}}{M} \int dz d\boldsymbol{\rho} \left| W_z(z) W_{\perp}(\boldsymbol{\rho} - \boldsymbol{\rho}_i) \right|^4, \quad (4)$$

where $\boldsymbol{\rho}$ denotes a two-dimensional vector in the $x - y$ plane and where W_z (respectively W_{\perp}) are the Wannier functions for the vertical (resp. horizontal) lattice potential. The scattering length a_{gg} describes low-energy s -wave scattering between two atoms in the internal state g , and has been measured in [20], $a_{gg} = 105(2) a_0$ with a_0 the Bohr radius. Using collapse and revival dynamics (see [21] and appendix A), we measure $U_{gg}/\hbar = 1475(25)$ Hz, which compares well with the value 1420 Hz calculated from Eq. 4 using the calibrated lattice depths. Unless otherwise mentioned, the quoted error bars represent a 68% confidence interval on the optimum fit value.

At zero temperature, the 2D Bose-Hubbard model supports phase transitions to incompressible Mott insulator (MI) phases [13, 22–24]. For a filling factor $\bar{n} = 1$, *i.e.* 1 atom per lattice site, Monte-Carlo simulations predict a transition for a critical value $(U_{gg}/J_{\perp})_c \approx 16.7$ [23], corresponding to HL depths around $V_{0,x} \approx V_{0,y} \approx 9 E_R$. The smooth harmonic trap V_T leads to a characteristic “wedding cake” density profile, *i.e.* density plateaus with integer filling, the denser plateaus occurring near the trap center [13]. In the present work, the HL depths become large enough at the end of the loading procedure so that we can safely neglect tunneling altogether ($J_{\perp} \approx 0$). Introducing a chemical potential μ , the spatial structure is then given, in the local density approximation, by

$$n(\boldsymbol{\rho}_i) = \text{Int} \left[\frac{\mu - \frac{M}{2} (\Omega_x^2 x_i^2 + \Omega_y^2 y_i^2)}{U_{gg}} \right] + 1, \quad (5)$$

where $\text{Int}(x)$ denotes the integer part of x . For finite temperatures and/or tunneling (still small compared to U_{gg}), the overall density profile remains similar but with smoother edges than predicted by Eq. 5. The relative weight of the plateau with \bar{n} atoms can be characterized by its reduced population (normalized to the total atom number), noted $\mathcal{F}_{\bar{n}}$ in the remainder of the article.

B. Single-atom Rabi oscillations on the clock transition

With a MI in the ground state g as a starting point, we now describe our experiments involving spectroscopy on the clock transition. In this section, we focus on the simplest case with only one atom per site. This can be realized by loading a sufficiently small number of atoms (such that only a plateau with $\bar{n} = 1$ atom per site appears) as in Fig. 2a, or by concentrating on the long time dynamics of Rabi oscillations as in Fig. 1b.

1. Optical setup

The optical setup has been presented in detail in [14]. Briefly, a laser resonant with the $g - e$ clock transition near $\lambda_0 \approx 578.4$ nm is locked on a high-finesse cavity well-isolated from its surroundings which serves as frequency reference. We split the optical path into one going to the cavity using an optical fiber with active Doppler noise cancellation [25], and the other going towards the atomic cloud. The wavevector \mathbf{k}_{cl} is oriented along the $\mathbf{e}_x + \mathbf{e}_y$ direction (see Fig. 1a).

The $g - e$ electric dipole transition is forbidden at zero field ($J = 0 \rightarrow J' = 0$ transition, with J the total electronic angular momentum). Following the method pioneered in [26, 27], we use a static magnetic field $\mathbf{B} = B_0 \mathbf{e}_z$ (with $B_0 \approx 182$ G) to enable an effective electric dipole coupling between g and e . Neglecting external degrees of freedom, the effective coupling strength is $\Omega_{\text{cl}} \propto B_0 \sqrt{I_{\text{cl}}}$ [26], where $I_{\text{cl}} = 2P_{\text{cl}}/(\pi w_{\text{cl}}^2)$, P_{cl} and w_{cl} are respectively the intensity, power and waist of the clock laser beam. For atoms in a deep optical lattice, the complete transition amplitude (hereafter denoted as “Rabi frequency” for simplicity) is $\Omega = \Omega_{\text{cl}} \times |\langle W_{\perp} | e^{i\mathbf{k}_{\text{cl}} \cdot \hat{\mathbf{r}}} | W_{\perp} \rangle|$, where the additional factor ≈ 0.9 takes into account the overlap between external states [1]. We find $\Omega \approx 2\pi \times 1500$ Hz using $I_{\text{cl}} \approx 2.6 \times 10^5$ mW/cm² ($P_{\text{cl}} \approx 20$ mW and $w_{\text{cl}} \approx 70$ μm) and a laser linearly polarized along \mathbf{e}_z , in good agreement with the measured value $\Omega \approx 2\pi \times 1450$ Hz for the experiment of Fig. 1b. Hopping transitions to different sites and to higher bands can be safely neglected (the Lamb-Dicke parameter is small, $(k_{\text{cl}} a_{\text{lat}})^2 \approx 0.08$ with $a_{\text{lat}} \approx 26$ nm the typical extent of the atomic wavefunction W_{\perp}).

2. Detection

We detect atoms in the ground state g using standard resonant absorption imaging on the $^1S_0 \rightarrow ^1P_1$ transition. Atoms in the excited state e are detected using a repumping laser on the $^3P_0 \rightarrow ^3D_1$ transition near 1389 nm. Here and in the remainder we denote by $N_{g/e}$ the atom number in the state g/e . The auxiliary 3D_1 state can decay to the 3P_J states ($J = 0, 1, 2$), where $^3P_{0,2}$ are metastable and where 3P_1 decays to the ground state by emitting a photon at 556 nm. The metastable 3P_2 state is a dark state for both the repumping and the imaging lasers. However, the branching ratio $^3D_1 \rightarrow ^3P_2$ is small [28], so that the repumping efficiency η_e from 3P_0 to 1S_0 is close to unity for a 500 μs -long repumping pulse. Comparing N_g and N_e for Rabi oscillations similar to Fig. 2a, we estimate $\eta_e \approx 80\%$, consistent with a calculation based on optical Bloch equations. In addition, atoms in the ground state are very far off-resonant and hardly affected. Hence, applying the repumping pulse allows us to detect the total population $N_g + N_e$ irrespective of the internal state. To detect selectively atoms in e and measure only N_e , we apply an additional 5 μs -long

removal pulse on the $^1S_0 \rightarrow ^1P_1$ transition before the repumping pulse. Atoms in g scatter many photons and are pushed away from the imaging region. Atoms in e are mostly unaffected by the removal pulse, although we measure a reduced detection efficiency by approximately 10%. This is possibly due to secondary scattering between trapped e atoms and untrapped g atoms leaving the sample. We have also observed a slight influence of the atomic density on the repumping efficiency. The observed efficiency is reduced by roughly 10% when N_e is higher than about 3×10^4 . Experimental atom numbers in e are not corrected for the efficiency but we do take it into account for the fits in Section III B and Section III C.

3. Single-atom dynamics

For atoms in singly-occupied lattice sites, the time evolution consists of textbook Rabi oscillations between g and e , described by the Hamiltonian

$$\hat{H}_{\text{eff}}^{(\bar{n}=1)} = \begin{bmatrix} 0 & \frac{\hbar\Omega}{2} \\ \frac{\hbar\Omega}{2} & -\hbar\delta \end{bmatrix}, \quad (6)$$

with $\delta = \omega_{\text{cl}} - \omega_0$ the laser detuning, $\omega_0 = 2\pi c/\lambda_0$ the atomic Bohr frequency of the transition, ω_{cl} the clock laser frequency and Ω the Rabi frequency introduced before. Starting from a sample in the ground state and switching on the coupling laser, the atomic populations oscillate between g and e at the frequency $\sqrt{\Omega^2 + \delta^2}$. In the remainder we characterize the coupling laser pulse by its duration T , or equivalently by its *area* ΩT . As seen from Fig. 1b, Rabi oscillations are damped for times larger than ~ 5 ms. In the following we discuss four possible damping sources.

We first consider frequency or intensity fluctuations of the clock laser. Although the intensity of this laser is not actively stabilized at the atomic cloud location, careful monitoring shows that intensity fluctuations remain below 1% and cannot explain the observed dephasing. Regarding frequency fluctuations, we have modeled their effect by a random detuning δ with a Gaussian distribution function of width $\Delta\omega_{\text{cl}}$. We have verified numerically that a width $\Delta\omega_{\text{cl}}$ of more than 600 Hz is required to account entirely for the observed damping. Narrower spectra presented in section 3.3 are not consistent with this value.

Additional dephasing mechanisms come from the spatial inhomogeneity of the coupling beam, leading to a non-uniform Ω . Moreover, the coupling beam also induces a position-dependent differential light shift, leading to a non-uniform δ [27]. These inhomogeneities cause a dephasing over time between the center and the edges of the cloud, and thus to an apparent damping when averaging over the whole cloud. We estimate numerically that a perfect centering of the clock beam on the atomic cloud would result in a dephasing time of approximately

20 ms, which is longer than the observed one. Although a displacement of 35 μm of the clock beam (half its waist) could fully account for the observed damping rate, this would entail a reduction of the maximum achievable Rabi frequency which we do not observe.

Another cause of inhomogeneous dephasing comes from a possible deviation from the exact magic wavelength, inducing a position-dependent differential light shift caused by the lattice potential. An order of magnitude estimation based on [16] indicates a differential shift across the cloud smaller than 10 Hz for a wavelength mismatch of 0.1 nm. Hence this effect can be neglected for the present work.

Additionally, we have recorded spectra at low atom numbers (to ensure almost unity filling across the cloud), π -pulse areas and long pulse times. When the pulse time exceeds ~ 5 ms, we observe substantial shot-to-shot fluctuations of the measured transition probability with identical parameters. This could be explained by a frequency jitter of the clock laser with a standard deviation of about 100 Hz, presumably due to the high-finesse cavity. This value can certainly be improved in future work.

We conclude that a combination of frequency fluctuations and inhomogeneous dephasing is likely responsible for the observed damping of the Rabi oscillations as in Fig. 1b. Nevertheless, we note that this damping has little influence on the shape and position of the spectra shown in Section III C, where the pulse time T is shorter than the damping time. However, the single-particle damping discussed in this paragraph limits the uncertainty on our measurement of collisional parameters presented in Section III C.

C. Determination of Mott shell populations

Fig. 1b illustrates that the temporal dynamics at early times can strongly differ from the Rabi oscillations expected for singly-occupied sites alone, as in Fig. 2a. While elastic interactions provide state-dependent energy shifts, inelastic interactions lead to a fast decay leaving only singly-occupied sites after ~ 1 ms (see Section III B). The long-time asymptote of $N_e + N_g$ in Fig. 1b thus reflects the initial fraction $\mathcal{F}_{\bar{n}=1}$ of atoms in singly-occupied sites of the MI phase. In Fig. 2b, we show the measured values of this asymptote for various initial atom numbers N_{at} .

In order to compare this measurement to the expected value of $\mathcal{F}_{\bar{n}=1}$ in a deep MI phase, we model the first phase of our loading sequence where the VL is quickly increased (see Section II A 2) using a sudden approximation. The initial atomic distribution for a BEC in the CDT is projected on a periodic potential of period $d = \lambda_{\text{m}}/2$ much smaller than the initial length L of the BEC. For a BEC in the Thomas-Fermi regime, this results in a distribution $N(z_k) \approx (1 - z_k^2)^2 (15N_{\text{at}}d)/(16L)\theta [1 - z_k^2]$ for the number of atoms in each plane of the VL at the altitude $z_k = kd/L$ (the integer k labels the plane), with

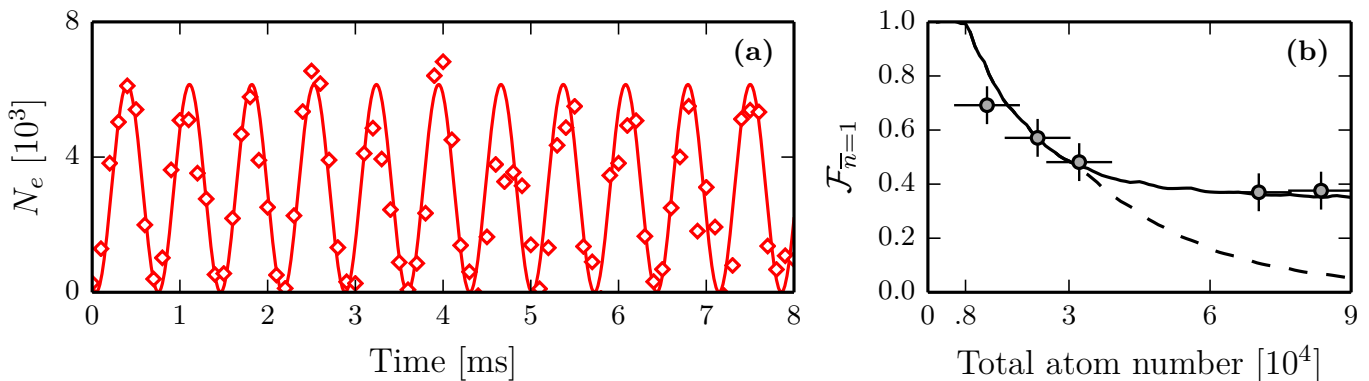


FIG. 2. **(a)** Rabi oscillations observed in e starting from a Mott insulator with only singly-occupied sites, prepared by reducing the total atom number to about 8×10^3 . Long-lived oscillations are observed in this case, without rapid initial decay. The solid line is a sinusoidal fit to the data. **(b)** Reduced population $\mathcal{F}_{\bar{n}=1}$ of the Mott shell with single occupancy. Data points are extracted from the asymptotic behavior of coherent oscillations as in Fig. 1b. The dashed line is the prediction from a model of our loading sequence assuming a perfect Mott insulator at zero temperature. The solid line also includes three-body collisions that quickly empty sites with triple occupation.

θ the Heaviside function. Using this distribution, we then assume a zero entropy sample in each plane, determined as the ground state of the 2D Bose-Hubbard model in Eq. 3 with $N(z_k)$ atoms. We finally compute the reduced populations summing over all k .

For the parameters of our experiment, there are typically $2L/d \approx 10 - 12$ occupied planes, with occupation numbers in a deep MI phase ranging from $\bar{n} = 1$ to $\bar{n} = 3$. For the lowest atom numbers explored in this work ($N_{\text{at}} \approx 8 \times 10^3$), we compute only a plateau with $\bar{n} = 1$, in agreement with Fig. 2a. For the largest atom numbers ($N_{\text{at}} \approx 8 \times 10^4$), we calculate plateaus with reduced populations $\mathcal{F}_{\bar{n}=\{1,2,3\}} = \{0.33, 0.46, 0.21\}$. The prediction of this loading model for the reduced population $\mathcal{F}_{\bar{n}=1}$, shown in Fig. 2b as dashed line, agrees with the measured values only for low atom numbers $N_{\text{at}} \lesssim 4 \times 10^4$.

The marked difference for higher atom numbers can be attributed to three-body inelastic losses, that occur at relatively high rates in optical lattices. We estimate a lifetime $\tau_{3B} \approx 100$ ms for triply-occupied sites using the three-body rate constant $L_3 \approx 7 \times 10^{-30}$ cm⁶/s measured in [29] (this lifetime is comparable to the loading time in the HL). A detailed kinetic modeling of these losses during the loading sequence is beyond the scope of this work. Here we extend our model in the simplest possible way, assuming that all triply-occupied sites have decayed

when the measurements are performed (the model predicts negligible population of sites with occupancy $\bar{n} > 3$, and we neglect them in our discussion). This assumption leads to the prediction $\mathcal{F}_{\bar{n}=1}/(\mathcal{F}_{\bar{n}=1} + \mathcal{F}_{\bar{n}=2})$ for the reduced population of singly-occupied sites (solid line in Fig. 2b). We find excellent agreement with the measured values. This supports the lossy loading model elaborated in this section and suggests that the in-trap density distribution is close to the expected one.

III. INTERACTING ATOMS DRIVEN ON THE CLOCK TRANSITION

A. Model

We now consider the dynamics of doubly-occupied sites driven by the coupling laser, which differs from singly-occupied sites in several aspects. First, due to bosonic enhancement, the coupling strength is $\sqrt{2}$ times higher for double than for single occupancy. Second, the three possible symmetric states $|gg\rangle$, $|eg\rangle$ and $|ee\rangle$ have in general different interaction energies, characterized by Hubbard parameters U_{gg} , U_{eg} and U_{ee} , the last two being unknown. Finally, the states $|eg\rangle$ and $|ee\rangle$ are prone to inelastic decay via principal quantum number changing collisions. We model this inelastic process by adding an imaginary term $-i\hbar\gamma_{e\alpha}/2$ to the Hamiltonian, with $\alpha = e, g$. This results in a dynamics captured by a non-Hermitian effective Hamiltonian

$$\hat{H}_{\text{eff}}^{(\bar{n}=2)} = \begin{bmatrix} 0 & \frac{\hbar\Omega}{\sqrt{2}} & 0 \\ \frac{\hbar\Omega}{\sqrt{2}} & U_{eg} - U_{gg} - i\frac{\hbar\gamma_{eg}}{2} - \hbar\delta & \frac{\hbar\Omega}{\sqrt{2}} \\ 0 & \frac{\hbar\Omega}{\sqrt{2}} & U_{ee} - U_{gg} - i\frac{\hbar\gamma_{ee}}{2} - 2\hbar\delta \end{bmatrix} \quad (7)$$

in the $\{|gg\rangle, |eg\rangle, |ee\rangle\}$ basis.

We numerically solve the generalized Schrödinger equation using the effective Hamiltonian Eq. 7 with initial condition $|\Psi^{(2)}\rangle = |gg\rangle$. We also solve the Schrödinger equation for singly-occupied sites using Eq. 6 with initial condition $|\Psi^{(1)}\rangle = |g\rangle$. This gives transition probabilities denoted $P_\alpha^{(2)} = |\langle\alpha|\Psi^{(2)}\rangle|^2$ with $\alpha = gg, eg, ee$ and $P_\beta^{(1)} = |\langle\beta|\Psi^{(1)}\rangle|^2$ with $\beta = g, e$. We then sum the contributions of doubly- and singly-occupied sites to obtain the average populations \bar{N}_g and \bar{N}_e , which we also measure using the methods described in Section II B 2. For example, we have

$$\frac{\bar{N}_e}{N_{\text{at}}} = \eta_e \mathcal{F}_{\bar{n}=1} P_e^{(1)} + \eta_e \mathcal{F}_{\bar{n}=2} \left(P_{ee}^{(2)} + \frac{1}{2} P_{eg}^{(2)} \right). \quad (8)$$

We assume the repumping efficiency η_e to be independent from the filling factor for simplicity.

B. Lifetime of doubly-occupied sites

Here we measure the inelastic loss rates γ_{ee} and γ_{eg} . We first investigate the role of $e-e$ inelastic collisions. After a coupling laser pulse of area $\Omega T = \pi$ in order to maximize the population in e , we switch off the coupling laser and apply a removal pulse (see Section II B 2) to get rid of atoms in state g . We are then left with a collection of singly- and doubly-occupied sites where all atoms are in the excited state e . We show in Fig. 3a the measured lifetime of this sample. We detect a fast exponential decay at short times which we interpret as the consequence of inelastic $e-e$ collisions. For longer times, we observe a plateau corresponding to the remaining e atoms in singly-occupied sites. The exponential decay rate is a direct measurement of $\gamma_{ee} = 9300(100) \text{ s}^{-1}$.

A similar technique is used to investigate the role of $e-g$ inelastic collisions. We apply a coupling laser pulse of area $\Omega T = \pi/2$ in order to maximize the population of $|eg\rangle$. We measure the atom number in the ground state g which is expected to decay as $\bar{N}_g/N_{\text{at}} = -\gamma_{eg} \mathcal{F}_{\bar{n}=2} P_{eg}^{(2)}/2$. Fig. 3b shows a typical measurement, where almost no losses occur even after 1 second. In order to extract a damping rate, we fix the initial populations using the previously described model in Section III A. An exponential fit to the data, with a rate γ as the only free parameter, yields $\gamma = 0.5(1) \text{ s}^{-1}$. The projected asymptote of the decay is represented with the dashed line in Fig. 3b. We measure a similar lifetime for atoms in g in the absence of the coupling laser. Hence the measured damping rate γ only gives us an upper bound for γ_{eg} .

C. Spectroscopy of elastic interactions

We now turn to the determination of elastic interaction parameters U_{eg} and U_{ee} . To this end, we perform spec-

troscopic experiments probing doubly-occupied sites, as explained in Fig. 4a-b.

The determination of U_{eg} is best performed in a perturbative limit, where the pulse area and the population of $|ee\rangle$ remain small (Fig. 4a). The time evolution of $|\Psi^{(2)}\rangle$ then reduces to that of a two-level system resonant for $\hbar\delta = U_{eg} - U_{gg}$. This resonance is well-resolved provided that the Rabi frequency is much smaller than $(U_{eg} - U_{gg})/\hbar$.

In order to extract the interaction strength U_{ee} , one could in principle use a two-photon resonance directly linking $|gg\rangle$ and $|ee\rangle$. This requires a weak enough Rabi frequency $\Omega \ll \Delta$ and $\delta' \ll \Delta$, where $\hbar\Delta = U_{eg} - (U_{ee} + U_{gg})/2$ is an interaction shift and where $\delta' = \delta - (U_{ee} - U_{gg})/(2\hbar)$ is the two-photon detuning. Under these conditions, the intermediate state $|eg\rangle$ can be adiabatically eliminated, and the dynamics reduces to that of an effective two-level system. Measuring the location of this two-photon resonance therefore allows one to determine $(U_{ee} - U_{gg})/2$. Practically, this idealized experiment is difficult to perform for weak coupling due to the strong loss rate γ_{ee} , which gives a substantial width to the two-photon resonance. In order to circumvent this issue, we perform the experiment at a larger Rabi frequency, and make use of the losses by measuring $N_g + N_e$ after a clock pulse of area $\Omega T = 2\pi$ (Fig. 4b). The ‘‘background signal’’ from singly-occupied sites is minimized near resonance, whereas doubly-occupied sites show a pronounced feature due to $e-e$ losses located at $\hbar\delta \approx (U_{ee} - U_{gg})/2$. Even for large Rabi frequencies, the loss spectral feature in the total signal is only weakly affected by the intermediate $|eg\rangle$ state (inset of Fig. 4b).

The experimental results are shown in Fig. 4c-d. Data is centered so that $\delta = 0$ corresponds to the single-atom resonance. The measurement of U_{eg} (Fig. 4c) is done with a weak Rabi frequency $\Omega^{\text{weak}}/(2\pi) \approx 150 \text{ Hz}$ and displays a ‘‘shoulder’’ near $\delta/(2\pi) \approx -300 \text{ Hz}$. This corresponds to the signal from doubly occupied sites. On the other hand, the measurement of U_{ee} (Fig. 4d), performed at strong Rabi frequency $\Omega^{\text{strong}}/(2\pi) \approx 1500 \text{ Hz}$, shows a loss peak almost coincident with $\delta/(2\pi) \approx 0 \text{ Hz}$, or equivalently $U_{ee} \approx U_{gg}$. To extract quantitative values, we fit the prediction of the model from Section III A to the experimental spectra shown in Fig. 4c-d, fixing the reduced populations $\mathcal{F}_{\bar{n}=1,2}$, the loss rates γ_{ee} , γ_{eg} and the initial atom number N_{at} to their measured values and leaving the Rabi frequencies Ω^{weak} , Ω^{strong} , the interaction energies U_{ee} , U_{eg} and the repumping efficiency η_e as free parameters. The prediction of the model has been further convolved with a Gaussian function to account for frequency jitter of the clock laser, the width σ being left as an extra free parameter. We obtain $\Omega^{\text{weak}}/(2\pi) = 145(13) \text{ Hz}$, $\Omega^{\text{strong}}/(2\pi) = 1470(70) \text{ Hz}$ and $\eta_e = 68(6) \%$, consistent with our calibrations. The width of the convolving Gaussian $\sigma = 100(40) \text{ Hz}$, is consistent with the narrowest spectrum we could observe, as discussed in Section II B 3. Finally we extract $(U_{ee} - U_{gg})/\hbar = -40(340) \text{ Hz}$ and $(U_{eg} - U_{gg})/\hbar =$

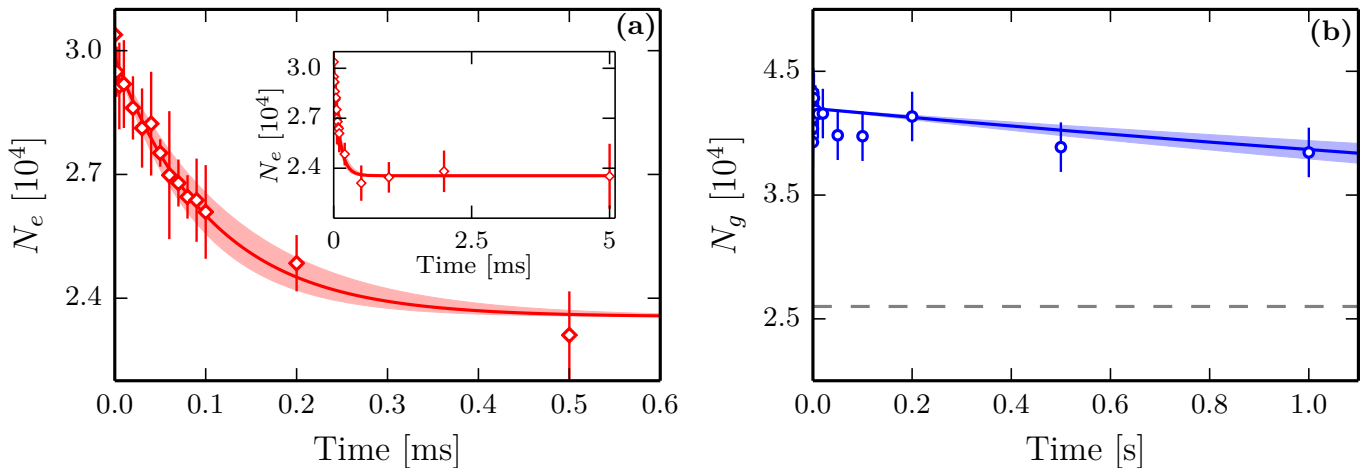


FIG. 3. **(a)** Lifetime measurement for a sample with only atoms in e . Doubly-occupied sites quickly decay through inelastic collisions. The inset shows the plateau of remaining singly-occupied sites for longer times. **(b)** Absence of inelastic collisions involving g and e . The dashed line shows the asymptote expected for a complete decay of $e - g$ pairs. In **(a)** and **(b)**, solid lines are exponential fits to the data, with the shaded area reflecting the 68% confidence intervals.

$-270(120)$ Hz, in agreement with the qualitative discussion above. The error bars represent statistical 68% confidence intervals on the optimal values of U_{eg} and U_{ee} , obtained by the bootstrap method.

D. Determination of atomic parameters

The ratio of the elastic interaction parameters U_{eg} and U_{ee} to U_{gg} is directly proportional to the ratio of the respective scattering lengths. From our calibration of U_{gg} (see appendix A) we get

$$a_{eg} - a_{gg} = -19(11) a_0, \quad (9)$$

$$a_{ee} - a_{gg} = -3(25) a_0. \quad (10)$$

The error bars do not account for possible systematic errors (for instance, in determining U_{gg}). Combining our measurements and the value $a_{gg} = 105 a_0$ from [20], we obtain the scattering lengths $a_{eg} = 86(11) a_0$, $a_{ee} = 102(25) a_0$.

We thus find all scattering lengths involving the clock states of ^{174}Yb equal within 20% [30]. The near-equality of the scattering lengths is somewhat surprising. These observations differ markedly from the fermionic ^{173}Yb isotope, where the equivalent scattering lengths have been found very different from one another [9, 10].

We also extract from the loss rate γ_{ee} the two-body loss rate constant β_{ee} that enters into the rate equation $d\langle\hat{\Psi}_e^\dagger\hat{\Psi}_e\rangle/dt = -\beta_{ee}\langle\hat{\Psi}_e^\dagger\hat{\Psi}_e^\dagger\hat{\Psi}_e\hat{\Psi}_e\rangle$ (the relation between the two is $\hbar\gamma_{ee}/U_{gg} = M\beta_{ee}/(4\pi\hbar a_{gg})$). We find

$$\beta_{ee} = 2.6(3) \times 10^{-11} \text{ cm}^3/\text{s}. \quad (11)$$

This value is in line with comparable measurements in strontium or fermionic ytterbium [10, 31, 32]. As noted in Section III B, we can only give an upper bound on the

rate constant $\beta_{eg} \leq 10^{-15} \text{ cm}^3/\text{s}$. Low $e - g$ inelastic loss rates were also observed for fermionic ^{173}Yb [10].

During the preparation of the manuscript, we learnt about similar experiments performed at LENS in Florence [33]. Their results agree with ours within the uncertainties.

IV. CONCLUSION

In conclusion, we have performed spectroscopy of a bosonic ytterbium Mott insulator using an optical clock transition. The high spectral resolution allows us to be sensitive to the on-site number statistics. Singly-occupied sites display long-lived coherent oscillations between g and e whereas the dynamics of doubly-occupied sites is strongly affected by two-body elastic and inelastic interactions. We extract the inelastic loss constants from lifetime measurements, and the elastic interaction parameters from spectroscopy. The resulting intra- and inter-states scattering lengths a_{gg} , a_{eg} and a_{ee} turn out to be very close to one another.

The large inelastic loss rate for two atoms in e at the same lattice site leads to sub-ms lifetimes. Such high rates are in line with measurements on other group-II atoms [31, 32], and are clearly a threat to experiments where such double occupancies can arise. Several solutions can be enforced to avoid this situation. If tunneling is irrelevant or detrimental (as in optical clocks), one can choose to work in a regime where only a Mott insulator with unit occupancy arises. This requires careful engineering of the auxiliary potential V_T , but it seems within current experimental capability even for a large atom number of several 10^5 . In a regime where tunneling cannot be neglected, one could imagine using an “interaction blockade”, where transitions to sites with double

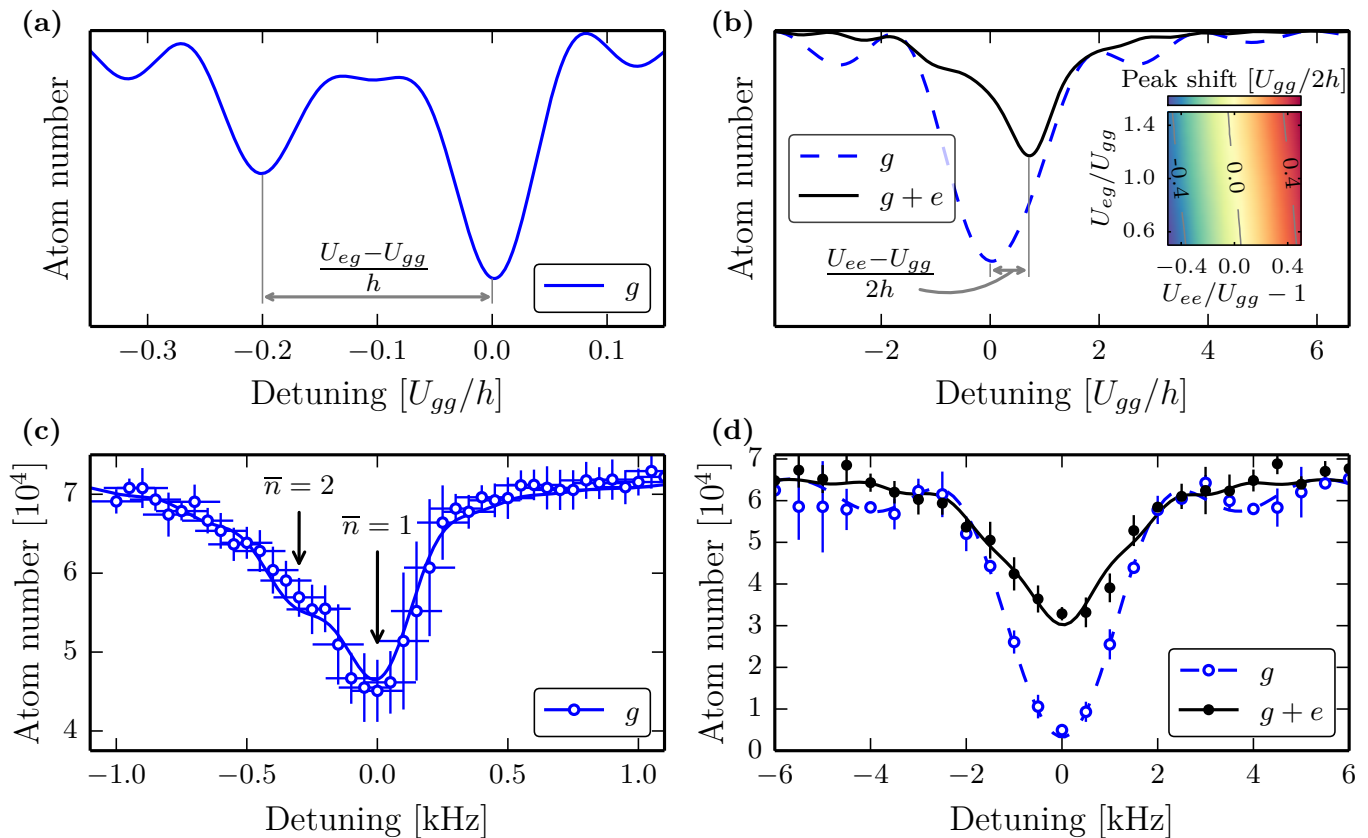


FIG. 4. Determination of U_{eg} and U_{ee} . In all plots, zero detuning corresponds to the single-atom resonance. (a) Method for measuring U_{eg} . For weak Rabi frequencies and pulse area $\Omega T = \pi$, an interaction sideband appears near $\delta = (U_{eg} - U_{gg})/h$, with δ the laser detuning. For illustrative purposes, $\Omega/(2\pi) = 70$ Hz and $U_{eg} = 0.8 U_{gg}$ in this plot. (b) Method for measuring U_{ee} . For strong Rabi frequencies and pulse area $\Omega T = 2\pi$, the total population of doubly occupied sites has decreased due to inelastic losses (black solid line). This loss resonance is shifted with respect to the single-atom resonance (dashed blue line, pulse area $\Omega T = \pi$) by $(U_{ee} - U_{gg})/(2h)$, with weak dependence on U_{eg} (see inset). For illustrative purposes, $\Omega/(2\pi) = 1500$ Hz and $U_{ee} = 2.5 U_{gg}$ in this plot. (c) Experimental determination of U_{eg} with $\Omega T \approx \pi$. The “shoulder” near $\delta/(2\pi) \approx -300$ Hz indicates the excitation of doubly occupied sites. (d) Experimental determination of U_{ee} . The open symbols show N_g for the reference measurement with $\Omega T \approx \pi$ locating the single-atom resonance. The closed ones correspond to $N_g + N_e$ for the loss measurement with $\Omega T \approx 2\pi$. The loss curve is almost centered on the single-atom resonance. A common fit to all data sets in (c) and (d) (solid and dashed lines) yields best fit parameters $U_{ee} = 0.97(23) U_{gg}$ and $U_{eg} = 0.82(8) U_{gg}$ (see text). The quoted error bars are statistical 68% confidence intervals obtained by the bootstrap method.

e occupancy will always be off resonant and thereby inefficient. The near-equality of a_{gg} , a_{eg} and a_{ee} for ^{174}Yb restricts this method to very low Rabi frequencies. Finally, the large inelastic rate suggests that the analog of the “quantum Zeno” suppression of losses [34–36] could occur in our system, where strong losses confine the system to a lossless subspace for a suitable initial state and weak enough coupling. This provides a natural direction for future work in a true Hubbard regime where both

interactions and tunneling play a role.

Acknowledgments: We thank M. Höfer and S. Fölling for discussions and for sharing their experimental results with us. We also thank G. Cappellini, J. Catani, L. Fallani and the LENS ytterbium team for stimulating discussions during the program “From Static to Dynamical Gauge Fields with Ultracold Atoms” (Galileo Galilei Institute, Florence). We are grateful to S. Nascimbène and J. Dalibard for their careful reading of the manuscript.

[1] A. D. Ludlow, M. M. Boyd, J. Ye, E. Peik, and P. O. Schmidt, Rev. Mod. Phys. **87**, 637 (2015), URL <https://link.aps.org/doi/10.1103/RevModPhys.87.637>.

[2] A. V. Gorshkov, A. M. Rey, A. J. Daley, M. M. Boyd, J. Ye, P. Zoller, and M. D. Lukin, Phys. Rev. Lett. **102**, 110503 (2009).

- [3] A. J. Daley, *Quantum Inf. Process.* **10**, 865 (2011), ISSN 1570-0755.
- [4] A. V. Gorshkov, M. Hermele, V. Gurarie, C. Xu, P. S. Julienne, J. Ye, P. Zoller, E. Demler, M. D. Lukin, and A. M. Rey, *Nat. Phys.* **6**, 289 (2010).
- [5] F. Gerbier and J. Dalibard, *New J. Phys.* **12**, 033007 (2010), URL <http://stacks.iop.org/1367-2630/12/i=3/a=033007>.
- [6] N. Goldman, F. Gerbier, and M. Lewenstein, *J. Phys. B: At. Mol. Opt. Phys.* **46**, 134010 (2013), URL <http://stacks.iop.org/0953-4075/46/i=13/a=134010>.
- [7] S. Kolkowitz, S. L. Bromley, T. Bothwell, M. L. Wall, G. E. Marti, A. P. Koller, X. Zhang, A. M. Rey, and J. Ye, *Nature* **542**, 66 (2017), ISSN 0028-0836, URL <http://dx.doi.org/10.1038/nature20811>.
- [8] L. F. Livi, G. Cappellini, M. Diem, L. Franchi, C. Clivati, M. Frittelli, F. Levi, D. Calonico, J. Catani, M. Inguscio, et al., *Phys. Rev. Lett.* **117**, 220401 (2016), URL <https://link.aps.org/doi/10.1103/PhysRevLett.117.220401>.
- [9] G. Cappellini, M. Mancini, G. Pagano, P. Lombardi, L. Livi, M. Siciliani de Cumis, P. Cancio, M. Pizzocaro, D. Calonico, F. Levi, et al., *Phys. Rev. Lett.* **113**, 120402 (2014).
- [10] F. Scazza, C. Hofrichter, M. Höfer, P. C. De Groot, I. Bloch, and S. Fölling, *Nat. Phys.* **10**, 779 (2014).
- [11] S. L. Campbell, R. B. Hutson, G. E. Marti, A. Goban, N. Darkwah Oppong, R. L. McNally, L. Sonderhouse, J. M. Robinson, W. Zhang, B. J. Bloom, et al., *A Fermi-degenerate three-dimensional optical lattice clock*, arXiv:1702.01210 (2017).
- [12] G. K. Campbell, M. M. Boyd, J. W. Thomsen, M. J. Martin, S. Blatt, M. D. Swallows, T. L. Nicholson, T. Fortier, C. W. Oates, S. A. Diddams, et al., *Science* **324**, 360 (2009), <http://www.sciencemag.org/content/324/5925/360.full.pdf>, URL <http://www.sciencemag.org/content/324/5925/360.abstract>.
- [13] I. Bloch, J. Dalibard, and W. Zwerger, *Rev. Mod. Phys.* **80**, 885 (2008).
- [14] A. Dureau, M. Scholl, Q. Beauvils, D. Döring, J. Beugnon, and F. Gerbier, *Phys. Rev. A* **91**, 023626 (2015).
- [15] M. Scholl, Q. Beauvils, A. Dureau, D. Döring, M. B. Aguilera, R. Bouganne, J. Beugnon, and F. Gerbier, in *2016 European Frequency and Time Forum (EFTF)* (2016), pp. 1–4.
- [16] Z. W. Barber, J. E. Stalnaker, N. D. Lemke, N. Poli, C. W. Oates, T. M. Fortier, S. A. Diddams, L. Hollberg, C. W. Hoyt, A. V. Taichenachev, et al., *Phys. Rev. Lett.* **100**, 103002 (2008).
- [17] V. A. Dzuba and A. Derevianko, *J. Phys. B: At. Mol. Opt. Phys.* **43**, 074011 (2010), URL <http://stacks.iop.org/0953-4075/43/i=7/a=074011>.
- [18] O. Morsch and M. Oberthaler, *Rev. Mod. Phys.* **78**, 179 (2006), URL <https://link.aps.org/doi/10.1103/RevModPhys.78.179>.
- [19] T. Gericke, F. Gerbier, A. Widera, S. Fölling, O. Mandel, and I. Bloch, *J. Mod. Opt.* **54**, 735 (2007), <http://dx.doi.org/10.1080/09500340600777730>, URL <http://dx.doi.org/10.1080/09500340600777730>.
- [20] M. Kitagawa, K. Enomoto, K. Kasa, Y. Takahashi, R. Ciuryło, P. Naidon, and P. S. Julienne, *Phys. Rev. A* **77**, 012719 (2008), URL <https://link.aps.org/doi/10.1103/PhysRevA.77.012719>.
- [21] M. Greiner, O. Mandel, T. W. Hänsch, and I. Bloch, *Nature* **419**, 51 (2002), ISSN 0028-0836, URL <http://dx.doi.org/10.1038/nature00968>.
- [22] I. B. Spielman, W. D. Phillips, and J. V. Porto, *Phys. Rev. Lett.* **98**, 080404 (2007), URL <https://link.aps.org/doi/10.1103/PhysRevLett.98.080404>.
- [23] B. Capogrosso-Sansone, i. m. c. G. Söyler, N. Prokof'ev, and B. Svistunov, *Phys. Rev. A* **77**, 015602 (2008), URL <https://link.aps.org/doi/10.1103/PhysRevA.77.015602>.
- [24] K. Jiménez-García, R. L. Compton, Y.-J. Lin, W. D. Phillips, J. V. Porto, and I. B. Spielman, *Phys. Rev. Lett.* **105**, 110401 (2010), URL <https://link.aps.org/doi/10.1103/PhysRevLett.105.110401>.
- [25] L. Ma, P. Jungner, J. Ye, and J. L. Hall, *Opt. Lett.* **19**, 1777 (1994), URL <http://ol.osa.org/abstract.cfm?URI=ol-19-21-1777>.
- [26] A. V. Taichenachev, V. I. Yudin, C. W. Oates, C. W. Hoyt, Z. W. Barber, and L. Hollberg, *Phys. Rev. Lett.* **96**, 083001 (2006), URL <https://link.aps.org/doi/10.1103/PhysRevLett.96.083001>.
- [27] Z. W. Barber, C. W. Hoyt, C. W. Oates, L. Hollberg, A. V. Taichenachev, and V. I. Yudin, *Phys. Rev. Lett.* **96**, 083002 (2006).
- [28] C. J. Bowers, D. Budker, E. D. Commins, D. DeMille, S. J. Freedman, A.-T. Nguyen, S.-Q. Shang, and M. Zolotarev, *Phys. Rev. A* **53**, 3103 (1996), URL <https://link.aps.org/doi/10.1103/PhysRevA.53.3103>.
- [29] T. Fukuhara, S. Sugawa, Y. Takasu, and Y. Takahashi, *Phys. Rev. A* **79**, 021601 (2009), URL <https://link.aps.org/doi/10.1103/PhysRevA.79.021601>.
- [30] Earlier, unpublished experiments obtained at LMU in Munich are consistent with our measurements [M. Höfer and S. Fölling, private communication, 2016].
- [31] A. Traverso, R. Chakraborty, Y. N. Martinez de Escobar, P. G. Mickelson, S. B. Nagel, M. Yan, and T. C. Killian, *Phys. Rev. A* **79**, 060702 (2009), URL <https://link.aps.org/doi/10.1103/PhysRevA.79.060702>.
- [32] A. D. Ludlow, N. D. Lemke, J. A. Sherman, C. W. Oates, G. Quémener, J. von Stecher, and A. M. Rey, *Phys. Rev. A* **84**, 052724 (2011).
- [33] L. Franchi, L. Livi, G. Cappellini, J. Catani, and L. Fallani, In preparation (2017).
- [34] N. Syassen, D. M. Bauer, M. Lettner, T. Volz, D. Dietze, J. J. García-Ripoll, J. I. Cirac, G. Rempe, and S. Dürr, *Science* **320**, 1329 (2008), <http://www.sciencemag.org/content/320/5881/1329.full.pdf>, URL <http://www.sciencemag.org/content/320/5881/1329.abstract>.
- [35] B. Yan, S. A. Moses, B. Gadway, J. P. Covey, K. R. A. Hazzard, A. M. Rey, D. S. Jin, and J. Ye, *Nature* **501**, 521 (2013), ISSN 0028-0836, URL <http://dx.doi.org/10.1038/nature12483>.
- [36] B. Zhu, B. Gadway, M. Foss-Feig, J. Schachenmayer, M. L. Wall, K. R. A. Hazzard, B. Yan, S. A. Moses, J. P. Covey, D. S. Jin, et al., *Phys. Rev. Lett.* **112**, 070404 (2014), URL <https://link.aps.org/doi/10.1103/PhysRevLett.112.070404>.
- [37] M. J. Martin, M. Bishof, M. D. Swallows, X. Zhang, C. Benko, J. von Stecher, A. V. Gorshkov, A. M. Rey, and J. Ye, *Science* **341**, 632 (2013), URL <http://www.sciencemag.org/content/341/6146/632.abstract>.
- [38] F. Dalfó, S. Giorgini, L. P. Pitaevskii, and S. Stringari, *Rev. Mod. Phys.* **71**, 463 (1999).

- [39] A. M. Rey, A. V. Gorshkov, C. V. Kraus, M. J. Martin, M. Bishof, M. D. Swallows, X. Zhang, C. Benko, J. Ye, N. D. Lemke, et al., *Ann. Phys.* **340**, 311 (2014), ISSN 0003-4916, URL <http://www.sciencedirect.com/science/article/pii/S0003491613002546>.
- [40] A. Yamaguchi, S. Uetake, S. Kato, H. Ito, and Y. Takahashi, *New J. Phys.* **12**, 103001 (2010), URL <http://stacks.iop.org/1367-2630/12/i=10/a=103001>.
- [41] X. Zhang, M. Bishof, S. L. Bromley, C. V. Kraus, M. S. Safronova, P. Zoller, A. M. Rey, and J. Ye, *Science* **345**, 1467 (2014), <http://www.sciencemag.org/content/345/6203/1467.full.pdf>, URL <http://www.sciencemag.org/content/345/6203/1467.abstract>.

Appendix A: Collapse and revival experiment

We have performed a collapse and revival experiment following [21] to determine experimentally the interac-

tion strength U_{gg} . We first prepare our system in a superfluid state by loading the atoms in a lattice with depths $V_{0,x} \approx V_{0,y} \approx 5 E_R$ and $V_{0,z} \approx 27 E_R$. Rapidly quenching the HL depths to $V_{0,x} \approx V_{0,y} \approx 26 E_R$ suppresses tunneling in the $x-y$ plane, and triggers a coherent interaction-driven evolution where first-order spatial coherence periodically collapses and revives with period h/U_{gg} (Fig. 5a-b). In a non-uniform system, the period of revivals is determined by U_{gg} alone (which can be taken uniform over the lattice with an error smaller than 1%), but the revival amplitude progressively decreases due to the inhomogeneous dephasing introduced by the spatial variation of the potential energy V_T across the cloud [21]. To extract the period without detailed modeling of the system, we fit equidistant Gaussian functions to our experimental data (Fig. 5b). In this way we account phenomenologically for the inhomogeneous damping [21].

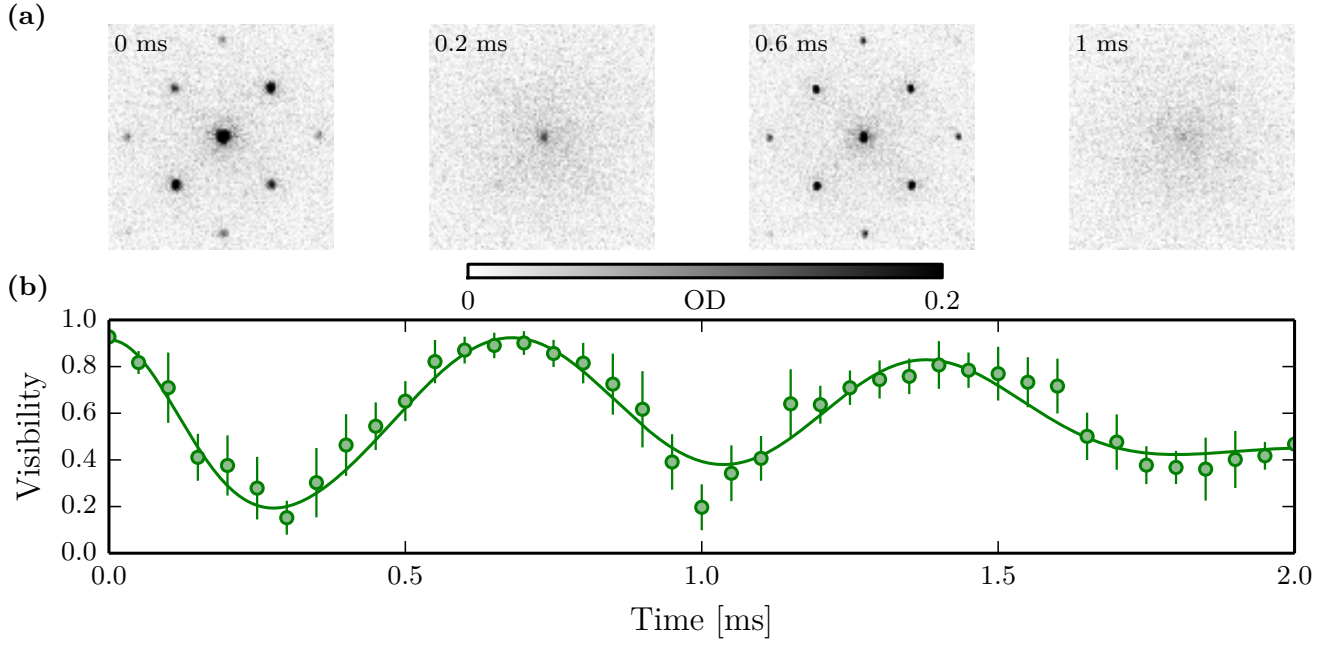


FIG. 5. **(a)** Experimental images of the interference pattern at different hold times after quenching the HL. **(b)** Visibility of the interference pattern undergoing collapse and revival dynamics. The period of the revivals is given by the on-site interaction energy U_{gg} . The solid line is a phenomenological fit using a sum of equidistant Gaussian functions giving $U_{gg}/h = 1475(25)$ Hz.